Airborne UWB FMCW Radar for Snow Depth Measurements

Shriniwas Kolpuke[1,2], *Member, IEEE*, Christopher D. Simpson[1,2], *Member, IEEE*, Feras Abushakra[1,3], Abhishek K. Awasthi[1,3,5], *Member, IEEE*, Omid Reyhanigalangashi[1,3], *Member, IEEE*, Jacob Pierce[1,2], Tuan Luong[1,2], Jordan Larson[1,2], *Member, IEEE*, Drew Taylor[1,3], *Member, IEEE*, David Braaten[4], *Member, IEEE*, Prasad Gogineni[1,2,3], *Life Fellow, IEEE*

Abstract—We developed and deployed a high sensitivity and low transmit power airborne UWB FMCW radar for snow depth measurements. The radar has a near-ideal point target response so that we can produce near-real-time snow thickness maps after each survey flight. The improved performance is achieved by carefully designing the radar hardware to reduce internal reflections between various components, third-order products generated by mixers, higher-order harmonics generated in multipliers and non-linear devices, and amplitude and phase errors in transmitted chirp signals. In addition, we performed extensive linear and non-linear system simulations to predict degradations in the radar hardware in advance and applied the remedies to correct them. These improvements allowed for near-real-time data products to be generated by reducing the need for advanced signal processing techniques. We also developed a T-shape Mills-Cross antenna array to obtain a small overlapped footprint of transmit and receive antennas. We performed measurements over snow in Grand Mesa, Colorado, from March to April 2022, and the radar mapped the top and bottom interfaces and density changes of 1.2-2.1m of snow. We generated a snow thickness map from the data collected over the grid flown and compared results with in-situ measurements. The comparison between radar estimates and in-situ measurements shows that the average snow depths obtained from the radar data are within a standard deviation from the mean of in-situ measurements.

Index Terms— FMCW Radar, Phase Errors, Phase Corrections, RF Chirp nonlinearity, Snow measurements, Snow depth map.

I. INTRODUCTION

THE Colorado River Basin (CRB) gets 75% of its water from snow melt. It constitutes the water supply of 40 million people in seven states, two countries, and 5.5 million irrigated acres of land [1, 2]. The primary reservoirs on the Colorado River—Lake Mead in the lower basin and Lake Powell in the upper basin—which allow storage of approximately four times the annual runoff, are facing historic drought conditions. According to the United States Bureau of Reclamation data, Lake Mead dropped to a historic low of 1040.92 feet in July 2022 [3]. This drop in water levels affects the electricity generation and freshwater supply to multiple Western states. According to economists [4], the water from the CRB region supports $1.434 trillion in gross state products and 16 million jobs in Arizona, Colorado, Nevada, New Mexico, California, Utah, and Wyoming. This economic activity constituted one-twelfth of the total U.S. gross domestic product (GDP) in 2012. The unavailability of Colorado River water to residents, businesses, industry, and agriculture can cause a loss of 64.4% of the CRB Region's annual GDP. Therefore, an accurate water availability assessment is crucial to regional water managers who allocate available water among varied stakeholder demands [2]. Similarly on the global scale, more than one-sixth of Earth's population relies on glaciers and seasonal snowpacks for their water supply [5].

The operational snow water equivalent (SWE) and snow depth measurements from the United States Natural Resource Conservation Service's (NRC) SNOw TELemetry (SNOTEL) network are available in real-time for point scale [2]. However, the snow depth is not constant in the local regions of concern, and the melt rate varies significantly. Therefore, more accurate information with better resolution and an area snow depth map is essential for accurately estimating water availability. In addition, manual snow depth measurements are expensive, time-consuming, and potentially dangerous to the field crew, and the spatial intervals over which the snow depth can be measured manually are limited [6]. These limitations present the need for the use of remote sensing techniques.

Since the first conceptualization of the radar in 1925 by E. V. Appleton et al. [7] as well as patents and experiments followed by Jetson Bently [8] from General Electric Company in 1928 and Espenschied and Newhouse [9] from Bell Telephone Laboratories in 1938, the frequency-modulated continuous-wave (FMCW) radars have been extensively used for remote sensing applications. The first use of an FMCW radar for snow research can be traced back to a series of papers

1. Remote Sensing Center, The University of Alabama, Tuscaloosa, AL 35487, USA
2. Department of Aerospace Engineering and Mechanics, The University of Alabama, Tuscaloosa, AL 35487, USA
3. Department of Electrical and Computer Engineering, The University of Alabama, Tuscaloosa, AL 35487, USA
4. Department of Geography and Atmospheric Science, University of Kansas, Lawrence, KS 66045, USA
5. Department of Electrical and Electronics Engineering, School of Engineering, University of Petroleum and Energy Studies (UPES), Dehradun 248007, India

Corresponding Author: (e-mail: smkolpuke@ crimson.ua.edu).

from Ellerbruch et al. in 1977 [10], Boyne and Ellerbruch in 1979 [11], and Ellerbruch and Boyne in 1980 [12]; and the first successful demonstration of snow-water-equivalent (SWE) calculation from an FMCW radar can be attributed to them. The researchers used an 8-12 GHz X-band FMCW radar to measure the physical properties of snow, and they were able to calculate water equivalence from FMCW radar data to a ±5% accuracy. The first successful demonstration of measuring snow thickness over land and sea ice using an FMCW radar mounted on an aerial platform was conducted in the late 1990s and early 2000s by a team from The University of Kansas [13, 14]. This FMCW radar operated from 2 to 6 GHz. Simultaneously, Kanagaratnam et al. [15], using an airborne 170 to 2000 MHz FMCW radar, measured internal snow layers in Greenland. Since then, several airborne radars have been researched and tested in the field. For example, Panzer et al. [16] proposed a UWB 2-8 GHz radar for snow measurement with 20 dBm output power. Similarly, Patel et al. [17] operated a Ku-band radar with a 6 GHz bandwidth covering 12-18 GHz.

M. J. Øyan et al. [18] presented a C-band airborne radar sounder with a 1 GHz bandwidth, 20 dBm transmit power, and 15 cm range resolution. Yan et al. [19] presented three different approaches for the FMCW radar and showed measured responses using the Hanning window. In the YIG (yttrium iron garnet) oscillator-based approach, which employs an operating frequency of 2-8 GHz, in the measured response, the first sidelobe appears around 30 dB below the primary lobe but has various reflections and products going as high as -24 dB. In the VCO-based approach, which employs an operating frequency of 2-8 GHz, the measured response has side lobes of about 20 dB below the main lobe. The final DDS-based system measured response for the 2-8 GHz shows sidelobes around -24 dB for the pre-distorted signal and -20 dB for the original signal. Yan et al. [20] proposed a wideband 2-18 GHz range to achieve a range resolution of 1.4 cm with 34 dBm transmit power and 0.05% non-linearity. The measured radar response for this system shows the first sidelobe at -13 dB from the main lobe using a Hanning window. Rodriguez-Morales et al. [21] presented a 2-18 GHz radar that achieved a 1.4 cm range resolution with 30 dB transmit power and 0.00006% non-linearity. Additionally, J. Li et al. [22] developed a compact airborne radar that operated over 2-8 GHz for snow measurements and measured snow depth over Alaskan mountains and glaciers. This radar had its first side lobe at -25 dB and sidebands at -18 dB for a Hanning window.

Many platforms, e.g., UAVs, snow vehicles, crewed aircraft, and satellites, have been used to measure snow depth. Recently, Lievens et al. have shown the ability of the Sentinal-1 satellite to map snow depth in Northern Hemisphere mountains at $1km^2$ resolution [23]. However, even though the satellite platforms can cover large areas, the resolution is coarse for measurements over complex terrains. On the other hand, Tan et al. and Jessan et al. demonstrated the snow measurements using low-cost drone platforms with fine resolution [24-26]. Airborne platforms like DHC-6 Twin Otter give a unique advantage in bridging this gap and can cover broad areas with very fine resolution. A combination of manned aircraft with drones can provide both fine-resolution data over small areas and modest resolution data over large areas.

There is a direct relationship between the performance of the radar hardware and the amount of signal processing required to generate geophysical data products from radar data. If the radar generates spurious products, extensive signal processing is needed to remove these products. The time taken for additional signal processing of data significantly slows down the process of generating final data products and delivery for operational applications. It is possible to develop radars that provide almost perfect point target response by carefully designing each sub-system and system with recently available advanced simulation tools. The first such attempt to perform end-to-end radar simulations can be traced back to work by Kanagaratnam et al. in the early 2000s [27]. They were able to achieve a good match between simulated and measured results, but the bandwidth of their system was limited to about 300 MHz at a center frequency of 750 MHz.

We designed and developed a system that provides a near-ideal point-target response by simulating and optimizing each radar sub-system and integrated system. In an FM-CW radar, a beat-frequency signal proportional to the target range is generated by multiplying the received signal with a sample of the transmitter signal in a mixer. We reduced phase and amplitude errors introduced by the system by carefully matching transmitter and receiver paths to the mixer. We evaluated the performance using an optical delay line to simulate a point target. The first sidelobes of the measured response are within ~2 dB of an ideal point response. Furthermore, the linearity of 0.000028% is achieved for the transmit chirp using this optimized radar hardware and pre-distortion of the input chirp signal. We arranged the transmit and receive antenna arrays in a T-shaped Mills cross configuration to obtain a narrow antenna beam [28, 29, 30]. The effective two-way 3-dB antenna beamwidth is about 13^0. We performed these measurements over snow in Grand Mesa, Colorado, in April 2022. In this paper, we provide a detailed discussion of the radar system in section II, present antenna arrays used for airborne measurements and integrated radar hardware in section III, provide laboratory and field results in section IV, and present conclusions in the final section.

II. RADAR SYSTEM DESIGN

The transmit signal frequency of an FMCW radar is linearly swept as a function of time from start frequency (f_0) to stop frequency (f) over a bandwidth of (B) Hz. The phase of the transmit signal ($\emptyset(t)$) changes quadratically over the chirp duration (T). The transmit signal ($E(t)$) with amplitude ($A(t)$) can be expressed as:

$$E(t) = A(t)\, e^{\emptyset(t)} = A(t)\, e^{j\pi\left(2f_0 t + \frac{B}{T} t^2\right)} \qquad (1)$$

This frequency-modulated chirp signal is then transmitted toward a target and travels at the speed of light in free space. When the signal encounters a target, it reflects

some portion of its energy towards the source. When this signal reaches the receiver, it has traveled twice the range (r) between the target and radar and is delayed by (τ) seconds.

$$\tau = \frac{2\,r}{c} \qquad (2)$$

When we compare these transmitted and received signals, the difference (intermediate frequency signal after mixer operation) after taking a Fourier Transform generates a single frequency signal (f_b) that contains the information of the target. The RF mixer operation generates both sum and difference signals. An anti-aliasing low pass filter in the IF radar chain suppresses the sum signal product.

$$f_{\_} = \frac{B\tau}{T} \qquad (3)$$

This operation of the FMCW radar is explained in Fig. 1 for a point target. The ideal radar impulse response will have symmetric sidelobes: the first one at -31.47 dB [31] for received signal weighted with Hanning window; and the remaining far off sidelobes decay at a rate of 18 dB/octave for a point target as shown in Fig. 2. The width of the main lobe is inversely proportional to the bandwidth.
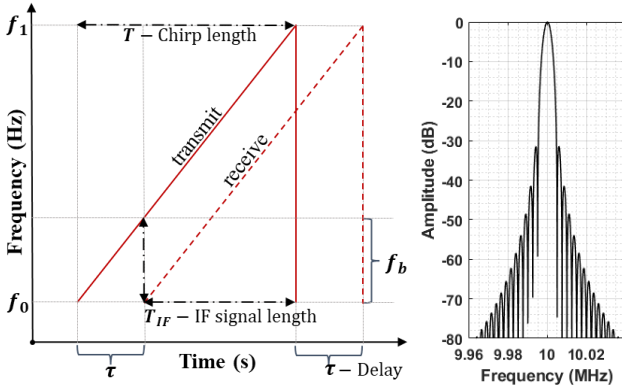

Fig. 1. FMCW radar operations and ideal Hanning window response.

Phase and amplitude errors are a major source of performance degradation in a radar. These errors can be present in the transmit signal or can be introduced by various RF components. Fig. 2 shows how different types of phase errors affect the ideal impulse response. Sinusoidal errors introduce ripples in phase or phase modulation of the beat-frequency signal. These errors will cause symmetric raised sidelobes in the impulse response for high-frequency (HF) terms and can cause asymmetric sidelobes for low-frequency (LF) terms. Cubic phase errors widen the main lobe, and a quartic phase error causes asymmetric sidelobes [32, 33].

The amplitude modulation on the chirp signal introduces symmetric raised sidelobes in the impulse response, much like the sinusoidal phase error [32, 33]. Therefore, we minimized these errors in the radar transmit signal to achieve optimum performance.

(a)

(b)
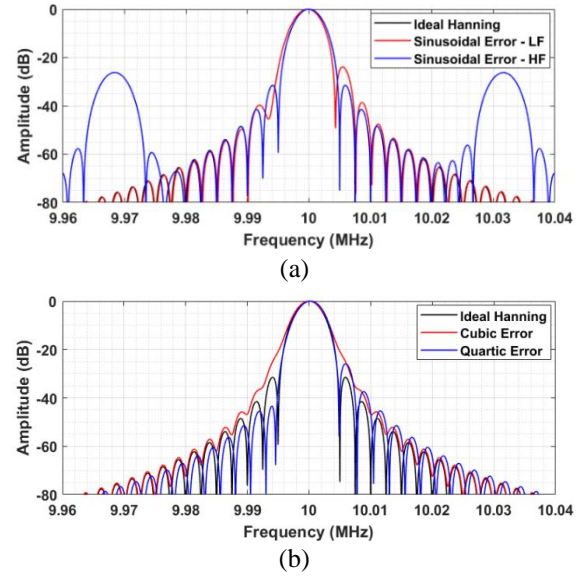
Fig. 2. Phase error effects comparison with ideal Hanning window: a) Sinusoidal phase error; b) Cubic and quartic phase error.
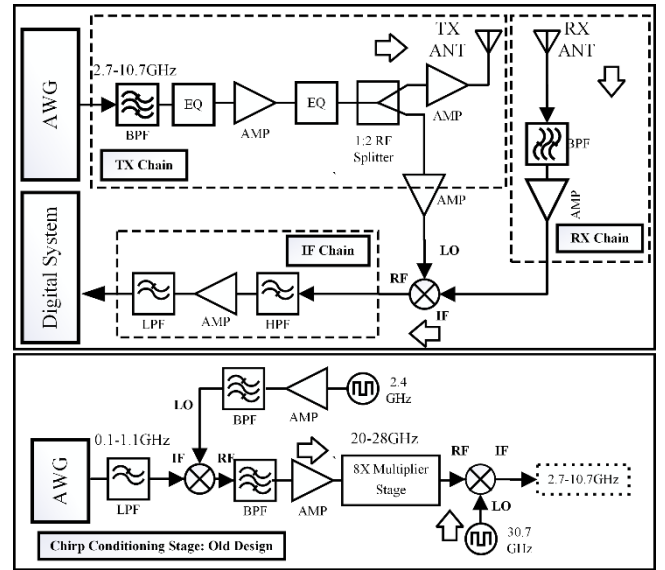
Fig. 3. The system architecture of the UWB FMCW radar.

The radar consists of four main subsystems: digital, RF, antenna, and DC power. The RF system consists of two main subsections: UWB chirp generation and radar transmit-receive module. Fig. 3 shows the system architecture of the FMCW radar (top) and the chirp conditioning stage (bottom). We analyzed two approaches to generating transmitter chirp signals. One of these generates a low-frequency (0.1-1.1 GHz) chirp using an arbitrary waveform generator (AWG) in the digital sub-system. The AWG generates a baseband chirp signal of 0.1-1.1 GHz with a 2.4 GHz sampling frequency. However, a chirp signal with 1 GHz bandwidth is insufficient to provide fine resolution measurements. Therefore, the chirp signal passes through the upconverter, frequency multiplier, and downconverter to obtain a UWB chirp of 8 GHz over the frequency range of 2.7 GHz-10.7 GHz. We define this as the

chirp conditioning stage.

The multiplier stage consists of three different RF chains connected consecutively on one board. The first chain contains a passive frequency doubler that is followed by a bandpass filter, amplifier, and reflectionless low-pass filter. This chain converts 2.5-3.5 GHz to 5-7 GHz. The second stage consists of a 2X active frequency multiplier and filters for converting a 5-7 GHz signal to 10-14 GHz. The final multiplier stage also consists of a 2X active multiplier and filters for converting 10-14 GHz to 20-28 GHz. A frequency doubler or multiplier output consists of a desired second harmonic and other frequency components, including the fundamental, higher harmonics as well as spurious products. The filters in the RF chains suppress these unwanted products. The second approach uses an external arbitrary waveform generator that can produce a direct chirp signal of 2.7-10.7 GHz with a 65 GHz sampling frequency.

The UWB chirp generated using the multiplication approach using mixers and multipliers results in nonlinearities and spurious higher-order products. In addition, the multiplication process causes degradations in the phase noise by a factor of $(20 \log_{10} N)$ [34]. The chirp signal will also be amplitude modulated by amplifiers and filters. The amplitude modulation results in symmetric sidelobes in the beat-frequency signal, and frequency-phase modulations result in asymmetrical sidelobes [32].

TABLE I
RADAR SYSTEM PARAMETERS

Quantity	Value	Units
Frequency	2.7 - 10.7	GHz
Range (Altitude)	200-650	m (Tested)
Chirp Length	140	µs
Pulse repetition interval	180	µs
Transmit Antenna Gain	18	dBi
Receiver Antenna Gain	15	dBi
Transmit Power	10	dBm (18 dBm max.)

We performed a thorough analysis of both approaches, identified shortcomings, and improved the radar performance to get a near-ideal response. Radar system parameters are shown in Table I. We achieved these improvements by performing extensive linear and non-linear simulations and used the simulation results to optimize the system. The improvement stages are presented in four steps as follows:

A. *Internal reflections in RF chains*

The internal reflections in the RF chains are due to the impedance mismatch between various components. If the mismatch is minor, then internal reflection does not affect the radar performance. We can predict internal reflections using S-parameters of individual components with an ideal FMCW transient simulation setup in Keysight ADS. Reflections in the radar will show up on the trailing edge of the impulse response and widen the main lobe if they are close to the primary target. First, each chain is optimized individually for internal reflections, which is achieved by carefully selecting and placing

components and adding attenuators between components to reduce multiple reflections. Fig. 4 shows the performance of various RF chains of this radar. The results are for the optimized chains, and their performance is close to the ideal Hanning response.
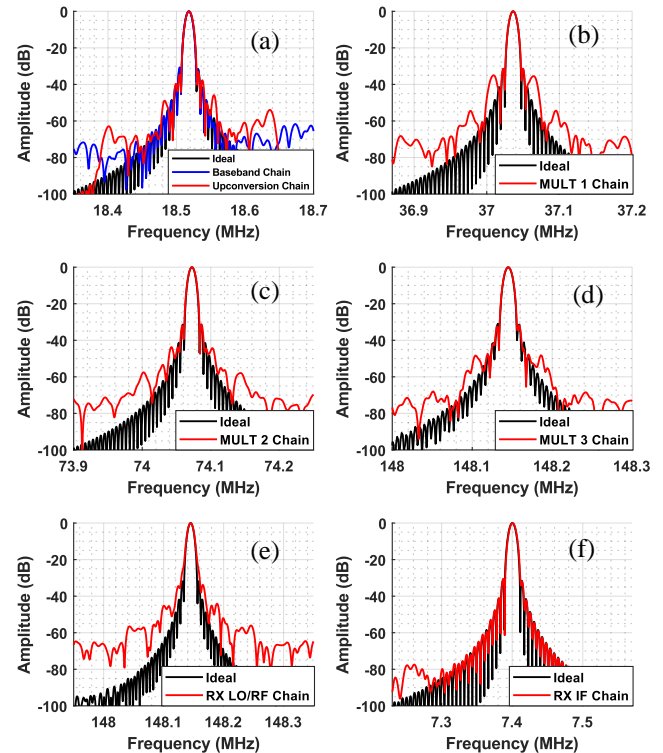

Fig. 4. Identifying degradations in the RF chains using Ideal FMCW setup using transient simulation in Keysight ADS: a) Baseband and upconverter, b) Multiplier #1, c) Multiplier #2, d) Multiplier #3, e) Receiver LO and RF, and f) Receiver IF chain.

Fig. 4 (a) shows the point target response at the baseband and after up-conversion. The upconverted signal matches the ideal response almost to the 50 dB level but has a slight asymmetry in the sidelobes due to the quartic phase error introduced by the sharp filter. The first multiplier stage (Fig. 4(b)) introduced two symmetrical sidelobes 37 dB below the main peak, caused by phase error introduced by filters. The second (Fig. 4(c)) and third (Fig. 4(d)) multiplier chains show similar sinusoidal error, but the lobes introduced are below 45 dB. The receiver LO and RF chain (Fig. 4(e)) show widening of the main lobe, which is caused by cubic phase error and raised symmetric sidelobes from the presence of sinusoidal phase error. The receiver IF chain shows a nearly ideal response in Fig. 4(f) with sinusoidal products being 80 dB below the main lobe.

It is essential to note that these plots represent the response of each RF chain for a perfect input with an ideal FMCW setup in the ADS software; therefore, the errors or non-ideal response of one chain is not contributing to the next one. However, in practice, these imperfections over several chains will accumulate and show up in the final response. The

This article has been accepted for publication in IEEE Transactions on Geoscience and Remote Sensing. This is the author's version which has not been fully edited and content may change prior to final publication. Citation information: DOI 10.1109/TGRS.2022.3223989

5

Keysight ADS recommends using the frequency multiplier module in the software for frequency domain (Harmonic balance) simulations only. Therefore, we could not perform the multiplication processes' time domain (transient) simulation, a process by which we could observe the accumulation of these errors in simulation.

B. Mixer and multipliers higher-order products

Another component that affects the radar performance is higher-order and inter-modulation products in the passband of the chirp signal. Higher-order products can be suppressed by a suitable filter design with sufficient attenuation in stopbands. Higher-order products are generally produced by nonlinear components such as multipliers and amplifiers. The mixers mainly produce inter-modulation products in the up-conversion and down-conversion processes. Harmonic Balance simulations can identify higher-order and inter-modulation products in Keysight ADS.
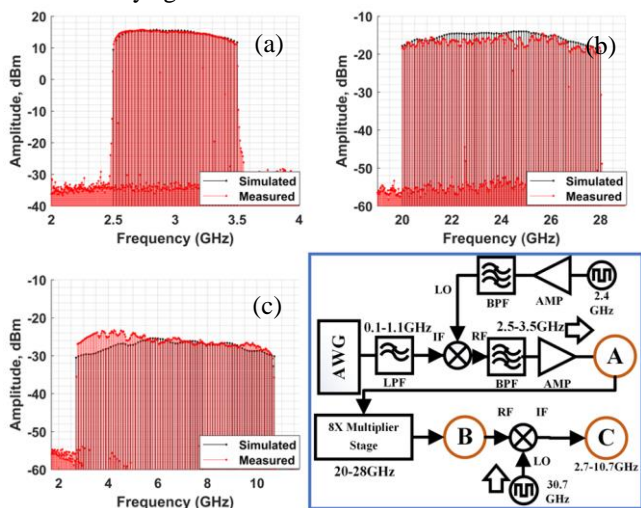

Fig. 5. Measured vs simulated spectrum at the output of various subsystems a) Up-converter chain, b) Multiplier chain, c) Down-conversion chain, d) Location of probing in the block diagram. The simulation results use the Harmonic balance simulator in Keysight ADS.

We successfully simulated and identified the higher-order and inter-modulation products and then designed appropriate filters and optimized multipliers by selecting input drive levels and padding to reduce out-of-band signals. As a result, most of the spurious signals are 40 dB below the desired 2.7-10.7 GHz chirp signal. Fig. 5 shows measured and simulated results for the upconverter (5a), multiplier (5b), and down-converter (5c). The measured results are within ± 1 dB of the simulated results for the upconverter, ± 2 dB for the multiplier, and ± 4 dB for the downconverter. The maximum disagreement between measured and simulated results occurred over the frequency range of 2.7-4.7 GHz. This mismatch is mainly because of the inaccurate modeling of the down-converter at the higher end of its frequency spectrum (26-28 GHz).

C. Matching LO and Tx-Rx Chains

The sharp cut-off filters used in the radar to remove out-of-band higher-order products introduce phase nonlinearities in transmitting chirp signals. These nonlinearities degrade the system point target response [29]. As discussed earlier, received signals are mixed with a sample of the transmit chirp signal to generate beat frequency signals proportional to the targets' range.

The sample of the transmit signal is used as the mixer local oscillator (LO). The system-induced phase nonlinearities can be reduced by matching the transfer function of the transmit-receive sub-section that supplies received signals to the mixer RF port and the transfer function of the sub-section that supplies a sample of the transmit signal to the mixer LO port. Fig. 6 shows the comparison of the matched and unmatched chains.
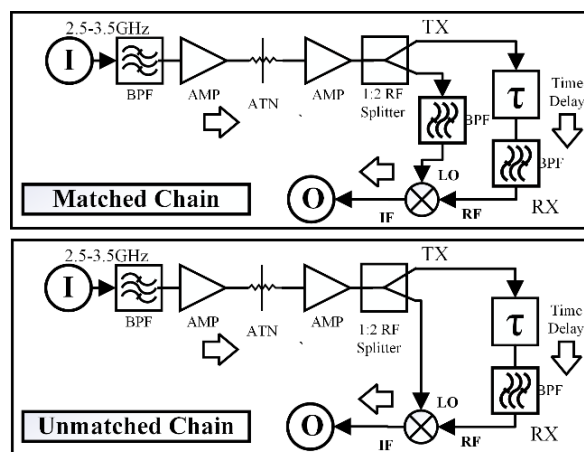
Fig. 6. Comparison of Matched and Unmatched chains - Block diagram of the ADS setup
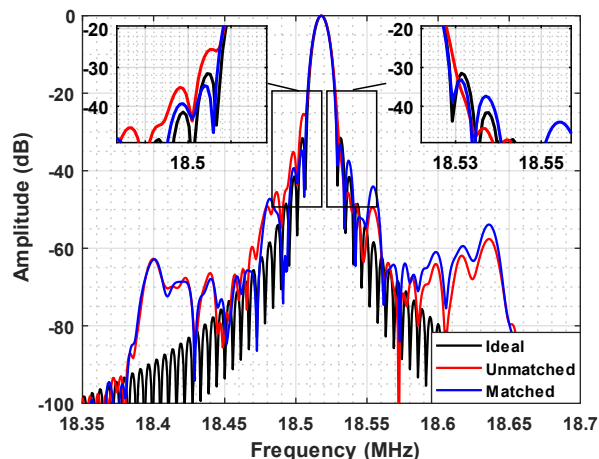
Fig. 7. Comparison of Matched and Unmatched chains - Impulse Response comparison. Simulated using the transient simulator in Keysight ADS.

Fig. 7 shows the simulated results with matched and unmatched paths for a Hanning window. The results for matched paths show the reduction of sidelobes introduced by phase errors. We can reduce these phase errors in the beat

frequency signal by matching the RF components used in the transmit-receive section to that of the LO. The LO sub-section can have more attenuation owing to the drive levels of the mixer if the additional attenuation does not introduce phase errors.

D. High-frequency (2nd and 3rd order harmonics) Signal Leakage and other products in beat frequency (IF) signal

Short duration transient signals introduced into the IF signal can degrade radar performance, as shown in Fig. 8 (a). These transient signals are coherent and have a broad spectrum covering the entire IF signal bandwidth. Unlike thermal noise, these signals cannot be reduced by coherent averaging. The experiments and analysis showed that these transient spikes are caused by the mixer's inter-modulation products generated from harmonics of LO/RF signals. We reduced these mixer-generated transients by reducing the LO drive level and incorporating an additional bandpass filter into the RF and LO ports of the mixer.

Fig. 8(a) shows the saturated noise floor during a delay line test with 75-dB attenuation resulting from the high amplitude leakage products, as seen in Fig. 8(b). We analyzed the short-duration signals both in the time and frequency domains. The expanded time-domain plots as a function of time are shown in Fig. 8(c) and 8(d). Fig. 8(e) shows the frequency domain response of these signals and Fig. 8 (f) shows the spectrogram of the same signals. These signals are caused by the 2nd and 3rd harmonics of the chirp present in RF and LO signals. To show that harmonics cause these signals, let us assume that the transmit chirp can be expressed as follows:

$$V(t)_{TX} = A_t e^{-j\left(\omega_0 t + \alpha \frac{t^2}{2}\right)} + B_t e^{-j(2\omega_0 t + \alpha t^2)} \quad (4)$$

The delayed received signal can be expressed as:

$$V(t)_{RX}^* = k\{A_r e^{j\left(\omega_0(t-\tau) + \alpha\frac{(t-\tau)^2}{2}\right)} + B_r e^{j(2\omega_0(t-\tau) + \alpha(t-\tau)^2)}\} \quad (5)$$
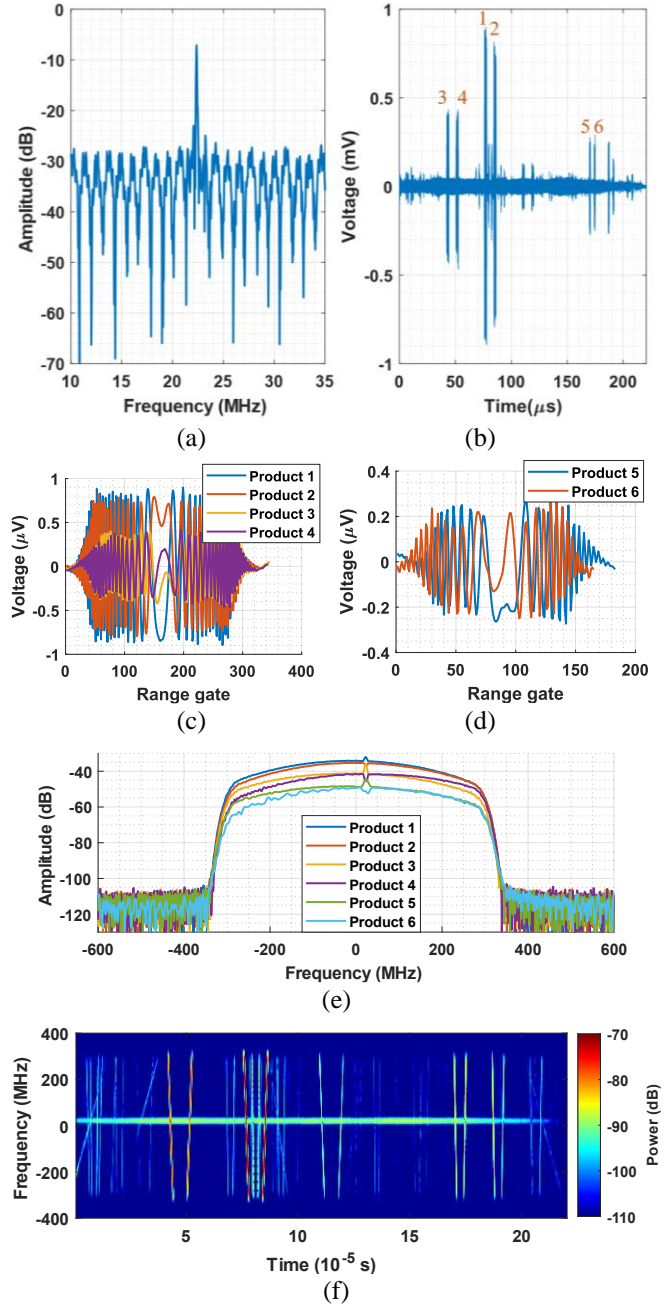
The IF Mixer output along with a filter to eliminate the sum frequencies can be expressed as:

$$V(t)_{IF} = V(t)_{TX} \times V(t)_{RX}^* \quad (6)$$

$$V(t)_{IF} = \left\{A_t e^{-j\left(\omega_0 t + \alpha\frac{t^2}{2}\right)} + B_t e^{-j(2\omega_0 t + \alpha t^2)}\right\} \times$$
$$k\left\{A_r e^{j\left(\omega_0(t-\tau) + \alpha\frac{(t-\tau)^2}{2}\right)} + B_r e^{j(2\omega_0(t-\tau) + \alpha(t-\tau)^2)}\right\} \quad (7)$$

Solving this further and ignoring the video phase terms $\alpha\frac{\tau^2}{2}$ and $\alpha\tau^2$, because $\tau \ll T$, we can separate main and cross products as follows:

$$V(t)_{IF\_main} = kA_t A_r e^{-j(\omega_0\tau + \alpha t\tau)} + kB_t B_r e^{-2j(\omega_0\tau + \alpha t\tau)} \quad (8)$$


Fig. 8. Results from radar (old design with chirp conditioning stage which uses RF multipliers) tests at 75 dB delay line attenuation: a) Impulse Response with saturated noise floor, b) Time-domain IF signal with chirp leakage products, c) Zoomed in and the selected portion of time-domain IF signal of products 1-4, d) Zoomed in and the selected portion of time-domain IF signal of products 5 and 6, e) Frequency-domain response of the selected products 1-6, and f) Spectrogram of the IF signal showing beat frequency signal at 22.36 MHz and the chirp leakage products.

$$V(t)_{IF\,cross\,products} = kA_t B_r e^{-j\left(-\omega_0 t + 2\omega_0\tau - \alpha\frac{t^2}{2} + 2\alpha t\tau\right)} +$$
$$kB_t A_r e^{-j\left(\omega_0 t + \alpha\frac{t^2}{2} + \omega_0\tau + \alpha t\tau\right)} \quad (9)$$

These cross-products are caused by higher-order harmonics of the transmit signal. They can be reduced by reducing the 2nd harmonic in the LO signal with suitable RF filters and using an IF reflection-less filter. After careful characterization and analysis, we reduced the cross-products by incorporating an additional RF filter to reduce the 2nd harmonic and an IF reflectionless filter.

E. Selection of the input signal

We compared the radar IF signal output responses for direct chirp input and chirp conditioning stage (multiplication approach) input to the transmitter-receiver section of the radar. Fig. 9 compares measured radar signal outputs for these two cases with the ideal response.
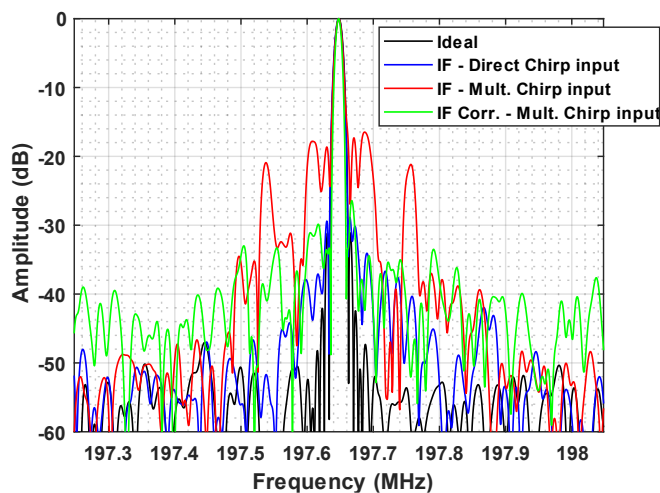

Fig. 9. The radar measured impulse response comparison

For the multiplication approach, the a) accumulation of phase and amplitude errors over the five RF chains, b) additional effects from the multiplier components, and c) phase error increase by ~18 dB ($20 \log_{10} 8$) due to a multiplication factor of eight have degraded the response significantly. In addition, the amplitude and phase corrections using pre-distortion were not feasible based on the output of the multiplication stages. However, they can be corrected in post processing, as shown in the Fig. 9. Therefore, to obtain an ideal point target response using chirp generated with frequency multiplication requires additional signal processing. On the contrary, with the direct chirp input, we can pre-distort the chirp to correct phase and amplitude errors and obtain close to an ideal point target response without additional signal processing. We decided to use direct chirp input for this field season based on these signal processing requirements because one of the requirements for our field program is to demonstrate that we can produce snow data products immediately after a flight. The use of a DHC-6 Twin Otter allowed us to utilize the heavier Keysight AWG with the capability to pre-distort the signal to correct for system errors to obtain a nearly ideal impulse response function.

III. T-SHAPE MILLS-CROSS ANTENNA CONFIGURATION AND INTEGRATED RADAR HARDWARE

We used a T-Shape Mills Cross antenna for a smaller footprint [30]. The transmit antenna has a narrow beamwidth in the along-track direction and a wide beamwidth in the cross-track direction. The receive antenna beamwidth is wide in the along-track and narrow in the cross-track direction. The combined pattern is a product of transmit and receive antenna patterns, as shown in Fig. 10.

For airborne measurements reported here, we used a coplanar Vivaldi antenna supported by a dielectric patch antenna that we reported in [35]. Each Vivaldi board has four elements. Herein, eight boards are used to constitute the transmitter and form a 4×8-element array. On the receive side, four boards are used as an 8×2-element array. The transmitter and receiver antennas are arranged in a T-shaped configuration, as shown in Fig. 11.
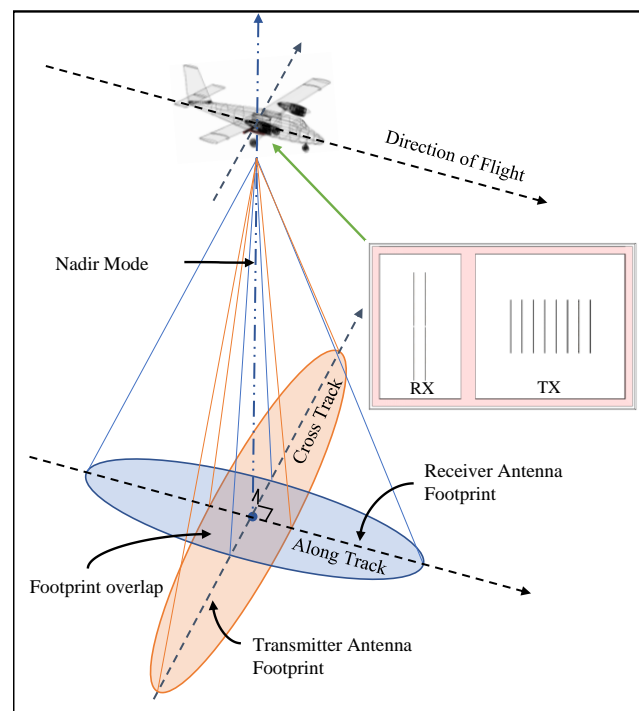
Fig. 10. The T-shaped antenna concept

The radome for antenna arrays is made from a lightweight and low-loss fiberglass material with 0.78 mm thickness. In addition, microwave absorbers were added to the corners to reduce reflections from the metal sheets and other radar components. Furthermore, we added a metal sheet between the transmitter and receiver and covered it with absorbers to improve the isolation. One of the major requirements to obtain high sensitivity with an airborne low-power FM-CW radar is high isolation between transmit and receive antennas. We obtained more than 50 dB isolation over the frequency range from 2.7 to 9 GHz and 40 dB above 9 GHz by careful design of the antenna housing and radome. The radar hardware and the power dividers needed for the antennas are mounted on the back of the antenna reflector plate. The narrow side of the main transmitter beam is orthogonal to the receiver.

This allows the overlapping antenna's footprint to be small and improves the SNR.

The DC voltage is supplied to the integrated box through an Amphenol connector. The radar control system is installed in the fuselage of the DHC-6 Twin Otter aircraft, and the final radar hardware integrated with the antenna structure is placed in the aft cavity of the aircraft. The integrated radar and antenna unit weighs ~16 lbs. The fuselage-mounted chassis weighs ~212 lbs. and includes the Keysight AWG, Arena Digital modules, UPS, display, and GPS modules. The addition of the chirp conditioning stage adds less than ~3 lbs. to the radar-antenna unit and eliminates the need for the Keysight AWG weighing ~30 lbs.


Fig. 11. Antennas-radar integrated unit during anechoic chamber test and radar control system rack mounted on DHC-6 Twin Otter aircraft.

The antennas are tested and measured to validate the results in the anechoic chamber. The s-parameters of the antennas are shown in Fig. 12, where the -10 dB reflection coefficient covers the band of 2.7-10 GHz, and the isolation between the transmit and receive antennas is more than 40 dB over the radar frequency range of operation. The radiation patterns at 4 GHz are also shown in Fig. 13. The 8×1 power divider used for the transmitter array is weighted by 3 dB at the edge elements to reduce the sidelobe level in the cross-track direction. The narrower side of the 3 dB point beamwidth for this antenna configuration is ~13° for transmitter and ~13° for receiver at lower frequency band.
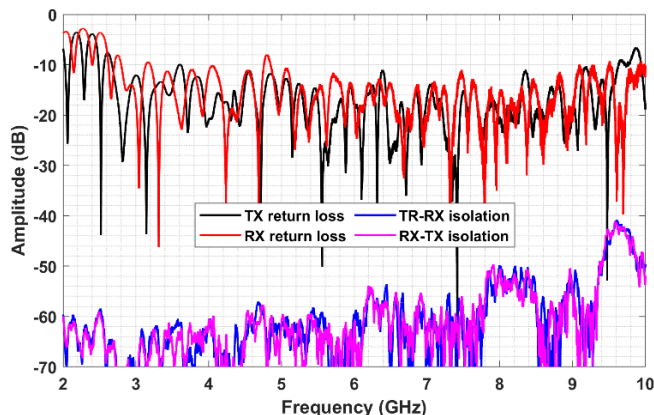
Fig.12. Measured S-parameters for the transmitter and receiver antennas.
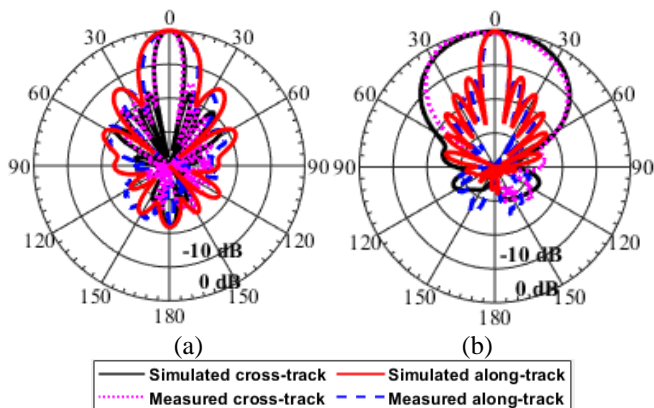
Fig. 13. The antenna's radiation pattern at 4 GHz (a) transmitter (b) receiver.

IV. MEASURED RADAR RESULTS

We performed laboratory measurements of the radar point target response and optimized its performance. We then integrated the radar on a Twin Otter aircraft and performed measurements on snow over Grand Mesa, Colorado, during the April 2022 deployment.

A. Laboratory testing

We evaluated the radar performance in the laboratory using an optical delay line to simulate a point target at a range of about 500 m. We also characterized the transmit signal amplitude and phase nonlinearities. First, we digitized transmit signal using a high-speed oscilloscope operating at a sampling rate of 65 GHz. Then, we used the digitized signal as an input to an ideal FM-CW radar simulated in MATLAB. Fig. 14(a) shows the ideal response in black and the digitized chirp response in red. The response shows that the chirp has amplitude and phase modulations that cause sidelobes much higher than those for an ideal chirp. The symmetrical sidelobes are caused by amplitude modulation, and small unsymmetrical

sidelobes are a result of phase errors. We estimated these errors and pre-distorted the transmit signal to obtain a nearly ideal point target response, which is shown in blue.
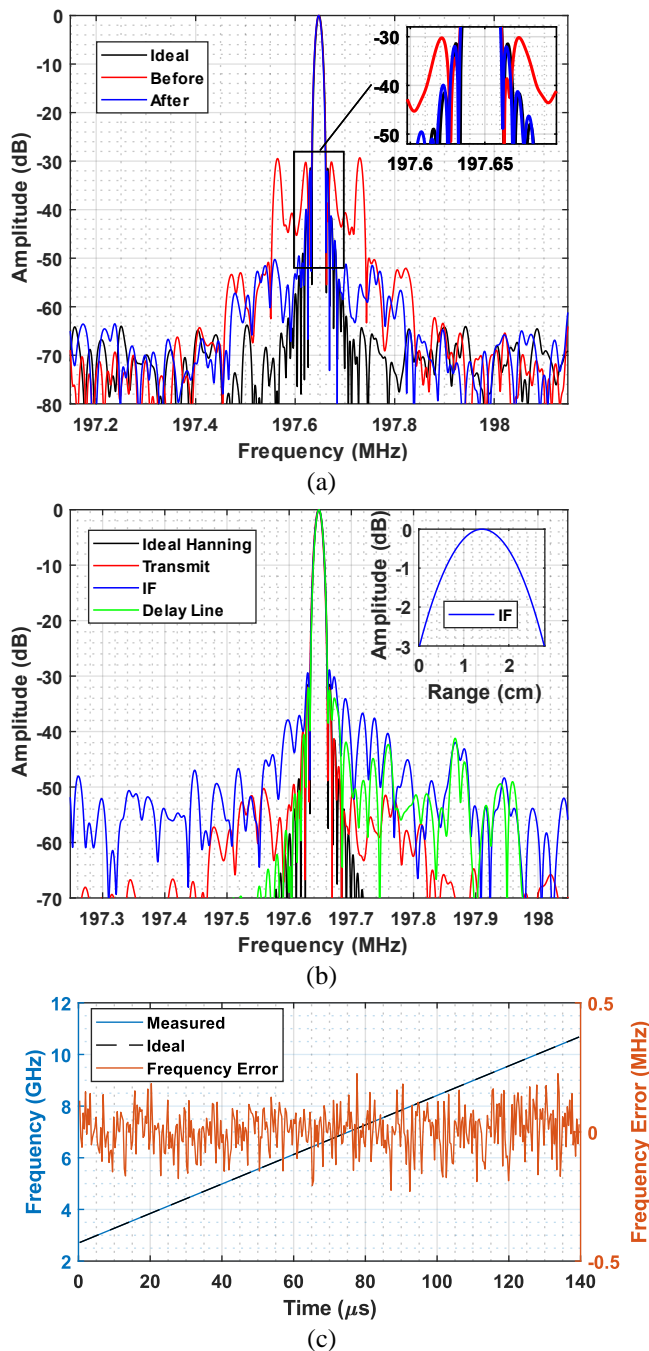

Fig. 14. The radar response for full band (2.7-10.7GHz): a) Impulse response comparison for original and pre-distorted chirp using ideal FMCW setup, b) Pre-distorted transmit chirp simulated impulse response comparison with the measured IF signal at 80 dB delay line attenuation and measured internal reflections of delay line, c) Linearity of the transmit chirp

We then used a 1-km (one-way) optical delay line to simulate a point target and characterize radar performance. Fig. 14(b) shows the radar's delay-line response (IF) along with the transmit signal response. The delay line results deviate from pre-distorted ideal system results because of small internal reflections in the delay line system. To verify this, we measured the delay line response using a calibrated vector network analyzer (VNA) and included it in Fig. 14(b). The large peaks at 197.87 MHz and 197.95 MHz are caused by a mismatch between components used to build the delay line. The deviations between VNA delay line response and radar response are caused by interference between sidelobes of the main response and sidelobes of the internal reflections on the trailing edge. However, these signals are 35 dB below the main peak.

The theoretical range resolution for this bandwidth using a Hanning window is 2.7 cm {1.44 $(c/2B)$}, and the measured range resolution for this radar at 3-dB points is 2.8 cm, as presented in Fig. 14(b). We used the corrected transmitter signal and compared it with the ideal chirp signal to calculate frequency deviation from a perfectly linear chirp. The linearity can be calculated with the peak deviation (Δf) and the total bandwidth (B) [36]. The calculation shows the signal has a linearity of 0.000028% as presented in Fig. 14 (c).

$$Linearity = \frac{\Delta f}{B} \tag{10}$$
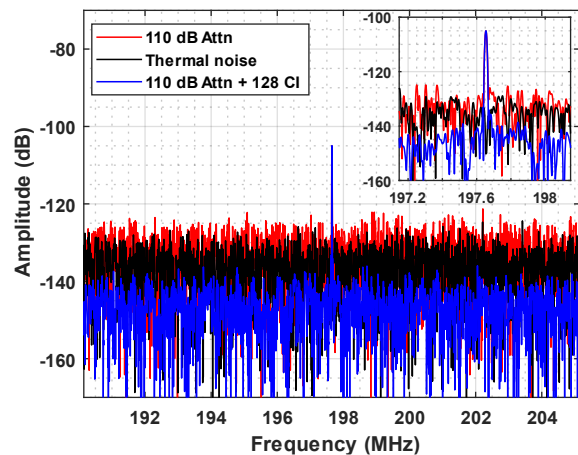
Fig. 15. The radar measured impulse response comparison at 110 dB optical delay line attenuation with the ADC thermal noise and expected SNR improvement of ~21 dB after 128 coherent integrations

We used coherent integration and synthetic aperture radar (SAR) processing to detect weak signals and improve along-track resolution. For data collected at 110 dB optical delay line attenuation, the radar signal has a signal-to-noise (S/N) of ~15 dB, and the noise floor is just ~2 dB above thermal noise. Theoretically, the signal-to-noise ratio must improve by ~21 dB with 128 coherent integrations. The results presented in Fig. 15 show a signal-to-noise ratio of ~36 dB after 128 coherent integrations. This confirms that the radar sensitivity is limited by thermal noise, not by coherent spurious signals.

B. Field Results

The snow on the Grand Mesa had already started

melting in April 2022, and the soil was visible on the edges of the Mesa. The central parts of the Mesa, where there is vegetation, still had a significant amount of snow, and we focused our measurements to include this region. Due to early melt conditions, we assumed that there was a small amount of liquid water present in the snow (~<5%) [37, 38]. We collected data over a grid covering 4.2 km by 6.6 km, with spacing of 600m between lines. The radar was flown at an altitude of about 500m above the surface for collecting data over the grid. we collected data over six days, and each mission lasted about 2-3 hours. The radar was calibrated with the delay line during turns at the start and end of each flight line. We also collected data over a smooth lake to determine radar response, including antenna arrays. We estimated the dielectric constant (ε_r) the relative density of dry snow (ρ_d) and wetness by volume (W_v) [35]:

$$\varepsilon_r = 1 + 1.7\,\rho_d + 0.7\,\rho_d^2 + 8.7\,W_v + 70\,W_v^2 \qquad (11)$$

Mesa Lakes Colorado SNOTEL Site reported a snow depth of 46 inches and snow water equivalent of 16 inches on the 8th of April, 2022 [39]. We computed snow density from SNOTEL data and assumed 2% of liquid water content to estimate the dielectric constant of snow as 1.85 for converting radar-measured electrical range into snow thickness.

Fig. 16. DHC-6 Twin Otter aircraft and aerial images of Grand Mesa, Colorado

For signal processing, we first read the raw radar data, hardware configuration, and DGPS files in MATLAB and then removed a few incomplete or lost data packets from the data sets before applying the coherent noise reduction algorithm. This consisted of coherently averaging several range lines of data and subtracting the average from each range line. The motion error correction occurs after the coherent noise reduction. The data are then processed with a SAR algorithm for FM-CW radars. We reduced speckle by incoherent averaging and applying a median filter to generate a final echogram. The layer tracker is employed to track the top air-snow interface and bottom snow-soil interface and calculate the snow depth. The snow thickness data are tagged with GPS data and used to generate a snow thickness map for the area. The near-ideal performance of the radar operating in the thermal noise region enabled us to generate usable final data products

within a few hours of the survey flight by eliminating the need for advanced deconvolution techniques. Fig. 16 shows the DHC-6 aircraft and aerial images of the Grand Mesa area in Colorado.


(a)

(b)
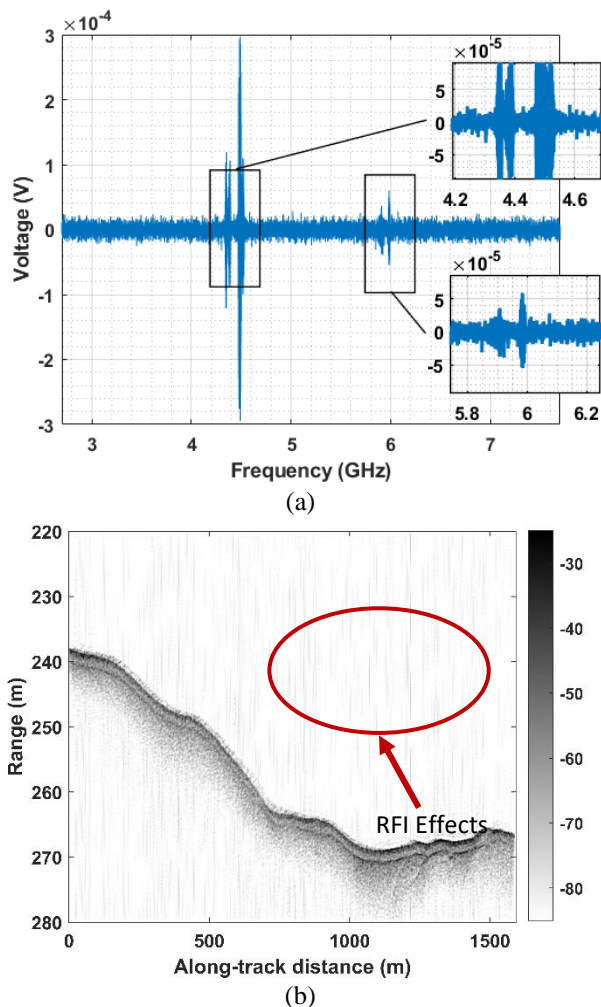
Fig. 17. RFI products a) Interfering products identified during the first test flight on 1st April 2022, b) Effect of small amplitude RFI on the Echogram form 7th April 2022 survey flight (2.7-4.2 GHz).

During the first test flight, we tried to characterize Radio Frequency Interference (RFI) signals in the frequency range of operation of the radar using a portable Keysight vector network/spectrum analyzer. However, it did not have adequate sensitivity to measure fast transient signals. Therefore, we configured the radar to capture transient RFI data. We accomplished this by operating it with a very low transmit power over the frequency range of 2.7-7.7 GHz and at a high altitude to keep reflected and scattered signals from the snow surface out of the IF low-pass filter passband. This allowed us to operate the radar in the thermal noise limited regime in the absence of RFI.

Fig. 17(a) shows measured RFI during the test flight. We observed large RFI signals over 4.3-4.4 GHz, which are probably caused by the aircraft radar altimeter, and low-

amplitude RFI signals over the frequency range of 5.6-6 GHz. The transient RFI signals cause vertical streaks in radar echograms after data are transformed into the frequency domain, as shown in Figure 17(b). This test allowed us to identify the unused frequency bands in the operating area of interest. We selected two frequency bands for collecting data over snow: 2.7-4.2 GHz (1.5 GHz bandwidth) and 4.8-7.3 GHz (2.5 GHz bandwidth). The range resolution for the lower frequency band is 14.4 cm in the air, and the higher frequency band is 8.64 cm in the air for the Hanning window.

The vertical streaks caused by incoherent RFI signals can be reduced by image processing radar echograms. By operating in the RFI free or low RFI regions of the spectrum, we did not have to perform any additional image processing of results reported here.

(a)

(b)
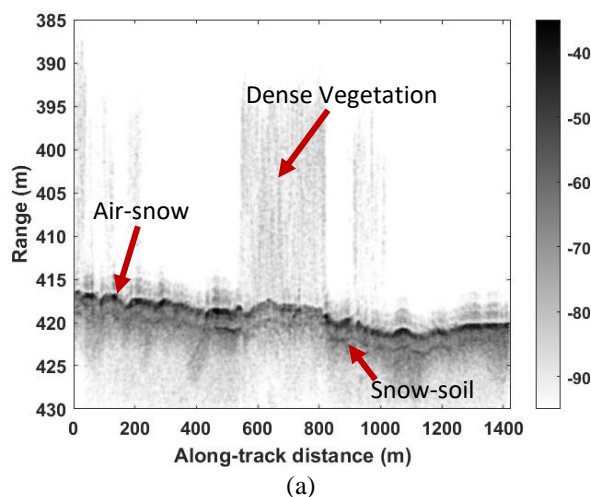
Fig. 18. Echogram from field tests a) Echogram from 15th April 2022 survey flight – electric range ($\varepsilon_r = 1$) using 4.8-7.3 GHz frequency band, b) Bing maps aerial image for the flight line

Despite these limitations on bandwidth, the radar collected excellent data showing the bottom layer in all the flight lines with just ~20 mW of transmit power. Moreover, the radar penetrated dense vegetation of 15-25 m and clearly showed the bottom snow-soil interface. Fig. 18(a) shows an echogram in which the bottom interface is visible in areas covered with 15-25 m tall trees. Figure 18(b) is a Bing Maps aerial image of the flight line area presented in radar echogram in Fig 18(a), showing dense vegetation. The start and stop points are from associated GPS data, but the dotted line is for representation only.
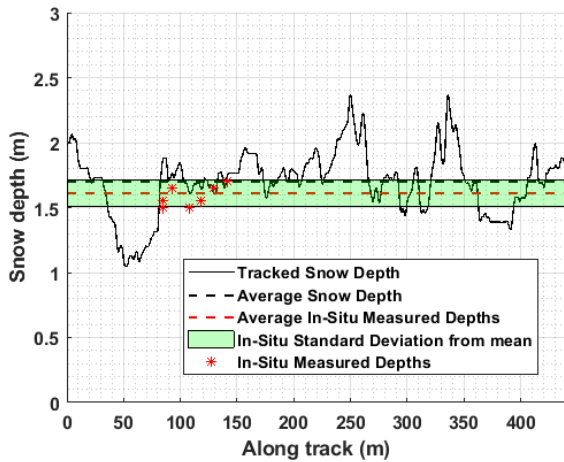

(a)

(b)
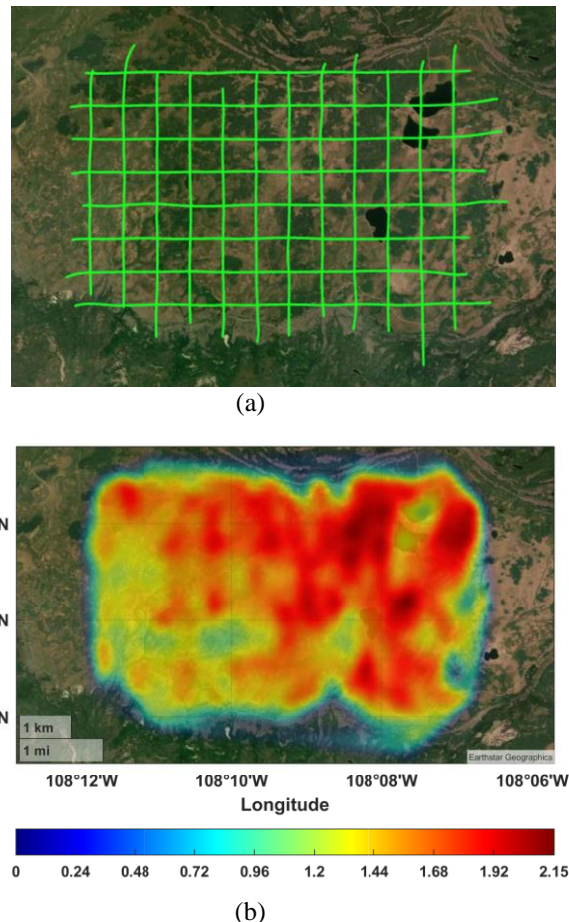
Fig. 19. Snow depth map from field tests a) Flight line grid, b) Area snow map for the flight grid on 8th April 2022 at $\varepsilon_r = 1.85$ using 2.7-4.2 GHz frequency band

The flight grid is shown in Fig. 19(a), and Fig. 19(b) presents the snow depth map of the area covered in the radar survey. The snow layer is thinning on water bodies and open patches; however, the melt rate is lower in the vegetated areas resulting in higher snow depth. As a result, the natural snow depth variance is more than 1 m. Fig. 20 presents more example echograms with frozen water bodies and dense vegetation.

The in-situ measurement team could not access the flight grid area in a standard vehicle, so we flew over area they collected in-situ measurements for the drone radar that we deployed over Grand Mesa on April 1, 2022. The in-situ measurement points are roughly 120 m away from the actual flight line, so we projected the depth measurements on the flight line data in the north-south direction. The comparison in Fig. 21 shows that the average snow depth obtained from the radar data is within the standard deviation of the mean of in-situ measurements.
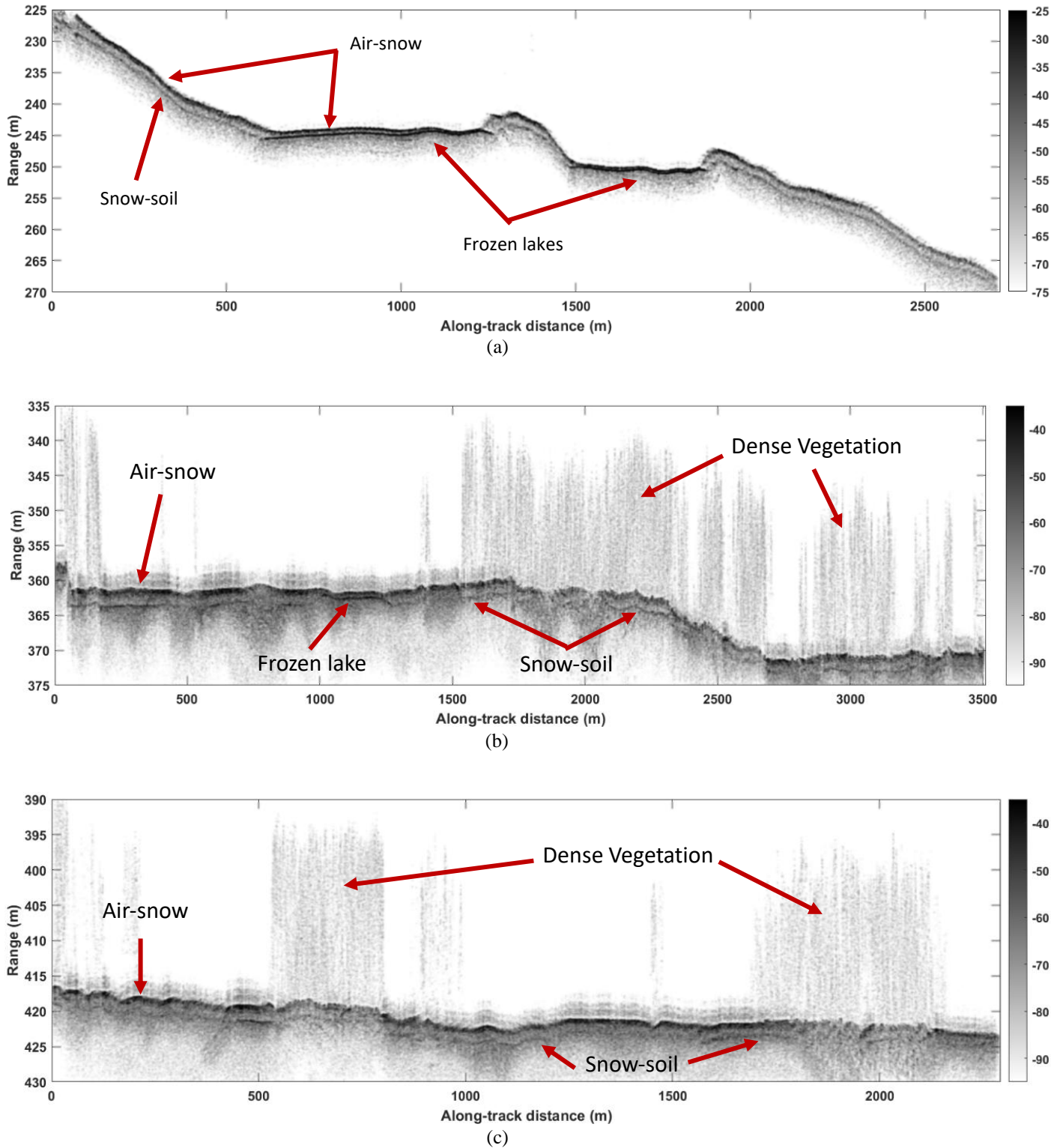
Fig. 20. Echograms from the field deployment for electric range ($\varepsilon_r = 1$): a) Flight line on the frozen lake on 7th April 2022 (2.7-4.2 GHz), b) Flight line with dense vegetation and frozen lake on 15th April 2022 (4.8-7.3 GHz), c) Flight line with dense vegetation on 15th April 2022 (4.8-7.3 GHz)

This article has been accepted for publication in IEEE Transactions on Geoscience and Remote Sensing. This is the author's version which has not been fully edited and content may change prior to final publication. Citation information: DOI 10.1109/TGRS.2022.3223989

13

Fig. 21. In-situ measurements comparison with the snow depth measured from radar flight

Based on our tests and analysis, we can see the bottom snow-land interface layer clearly up to a terrain slope of about 4°. An UWB radar detection of snow-air and snow-land interfaces is based on strong quasi-specular or coherent returns from these interfaces. The coherent returns from the bottom interface decay very rapidly with incidence angle [40] and can be masked by the snow surface and volume backscatter, referred to as clutter here. By estimating the average clutter over an area and subtracting it from each line of data in the echogram, we can reduce the clutter and bring out returns from the bottom interface [41]. The backscattered signals, referred to as clutter, can be reduced by SAR processing in the along-track direction and array processing in the cross-track direction [42-43]. We are upgrading the radar to include multiple receivers to digitize data from each element of the cross-track array for receive beam steering to recover quasi-specular returns.

V. CONCLUSION

We successfully designed, developed, and deployed a low-power high-sensitivity airborne UWB FMCW radar for snow measurements. We achieved an effective two-way 3 dB antenna beamwidth of 13° using T-shape Mills-Cross antenna array. The radar recently collected excellent data in Grand Mesa, Colorado, using only ~20-mW transmit power and less than one-fifth of its bandwidth capability. The radar shows the bottom layer for all flight lines and penetrates vegetation of 15-25 m to show the bottom snow-soil interface clearly. The radar data show thinning of the snow layer on water bodies and open patches; however, the melt rate is lower in vegetated areas resulting in higher snow depth. As a result, the snow depth variance detected is more than 1 m. The radar performance allowed us to generate usable data products within a few hours of each survey flight.

REFERENCES

[1] Deems, J. S., Painter, T. H., Barsugli, J. J., Belnap, J., and Udall, B.: "Combined impacts of current and future dust deposition and regional warming on Colorado River Basin snow dynamics and hydrology, " *Hydrol. Earth Syst. Sci.,* vol. 17, pp. 4401–4413, https://doi.org/10.5194/hess-17-4401-2013, 2013.

[2] Schneider, D., and Molotch, N. P. (2016), "Real-time estimation of snow water equivalent in the Upper Colorado River Basin using MODIS-based SWE Reconstructions and SNOTEL data," *Water Resour. Res.*, vol. 52, pp. 7892– 7910, doi:10.1002/2016WR019067.

[3] United States Bureau of Reclamation, Lower Colorado River Operations | Lower Colorado Region | Bureau of Reclamation (usbr.gov) (Accessed on:08/09/2022)

[4] James, T., Evans, A., Madly, E., & Kelly, C. (2014). The economic importance of the Colorado River to the basin region.

[5] Barnett, T., Adam, J. & Lettenmaier, D. "Potential impacts of a warming climate on water availability in snow-dominated regions," *Nature* vol. 438, pp. 303–309, 2005, https://doi.org/10.1038/nature04141

[6] Deems, J., Painter, T., & Finnegan, D. "Lidar measurement of snow depth: A review, " *Journal of Glaciology,* vol. *59*, pp. 467-479, 2015, doi:10.3189/2013JoG12J154

[7] Appleton, Edward Victor, Barnett, M. A. F. Larmor, Joseph, "On some direct evidence for downward atmospheric reflection of electric rays," 1925, Proceedings of the Royal Society of London. Series A, Containing Papers of a Mathematical and Physical Character, P 621-641, DOI:10.1098/rspa.1925.0149

[8] J. O. Bentley, "Airplane Altitude Indicating System, " 1935, United States Patient Office - 2011392

[9] Espenschied, L. and Newhouse, R.C. (1939), A Terrain Clearance Indicator*. *Bell System Technical Journal*, 18: 222-234. https://doi.org/10.1002/j.1538-7305.1939.tb00813.x

[10] Ellerbruch, D., Little, W.E., Boyne, H., & Bachman, D. (1977). "Microwave characteristics of snow" *45th Annual Western Snow Conference*, April 1977, Albuquerque, New Mexico.

[11] Boyne, H. S., and Ellerbruch D. A. (1979), "Microwave measurements of snow stratigraphy and water equivalence," *47th Annual Western Snow Conference*, April 1979, Sparks, Nevada, 1979.

[12] Ellerbruch, D., & Boyne, H. "Snow stratigraphy and water equivalence measured with an active microwave system," *Journal of Glaciology*, vol. 26, pp. 225-233, 1980.

[13] Gogineni, S., Wong, K., Krishnan, S., Kanagaratnam, P., Markus, T., & Lytle, V. "An ultra-wideband radar for measurements of snow thickness over sea ice' IGARSS 2003. *2003 IEEE International Geoscience and Remote Sensing Symposium. Proceedings* (IEEE Cat. No.03CH37477), vol. 4, pp. 2802-2804, 2003.

This article has been accepted for publication in IEEE Transactions on Geoscience and Remote Sensing. This article is the author's version which has not been fully edited and content may change prior to final publication. Citation information: DOI 10.1109/TGRS.2022.3223989

14

<

[14] P. Kanagaratam, S. P. Gogineni, N. Gundestrup and L. Larsen, "High-resolution monitoring of internal layers over the Greenland ice sheet," *IGARSS 2000. IEEE 2000 International Geoscience and Remote Sensing Symposium.* pp. 460-462, vol.2, 2000, doi: 10.1109/IGARSS.2000.861596.

[15] P. Kanagaratnam, R. Eakin and S. P. Gogineni, "An Airborne Radar System for High-Resolution Mapping of Internal Layers," *IGARSS '01*, pp. 940-942, 2001.

[16] B. Panzer et al., "An ultra-wideband, microwave radar for measuring snow thickness on sea ice and mapping near-surface internal layers in polar firn," *J. Glaciol.*, vol. 59, no. 214, pp. 244–254, 2013.

[17] A. Patel et al., "Fine-resolution radar altimeter measurements on land and sea ice," *IEEE Trans. Geosci. Remote Sens.*, vol. 53, no. 5, pp. 2547–2564, May 2015.

[18] M. J. Øyan, S. Hamran, L. Damsgård and T. Berger, "Compact Airborne C-Band Radar Sounder," in *IEEE Transactions on Geoscience and Remote Sensing*, vol. 52, no. 10, pp. 6326-6332, Oct. 2014, doi: 10.1109/TGRS.2013.2296074.

[19] J. -B. Yan et al., "Airborne Measurements of Snow Thickness: Using ultrawide-band frequency-modulated-continuous-wave radars," *IEEE Geoscience and Remote Sensing Magazine*, vol. 5, no. 2, pp. 57-76, June 2017, DOI: 10.1109/MGRS.2017.2663325.

[20] J. -B. Yan et al., "Ultrawideband FMCW Radar for Airborne Measurements of Snow Over Sea Ice and Land," *in IEEE Transactions on Geoscience and Remote Sensing*, vol. 55, no. 2, pp. 834-843, Feb. 2017, doi: 10.1109/TGRS.2016.2616134.

[21] F. Rodriguez-Morales et al., "An Improved UWB Microwave Radar for Very Long-Range Measurements of Snow Cover," in *IEEE Transactions on Instrumentation and Measurement*, vol. 69, no. 10, pp. 7761-7772, Oct. 2020, doi: 10.1109/TIM.2020.2982813.

[22] J. Li et al., "Airborne Snow Measurements Over Alaska Mountains and Glaciers With A Compact FMCW Radar," *IGARSS 2019 - 2019 IEEE International Geoscience and Remote Sensing Symposium*, 2019, pp. 3906-3909, doi: 10.1109/IGARSS.2019.8900034.

[23] Rolf Ole R. Jenssen and Svein Jacobsen, "Drone-mounted UWB snow radar: technical improvements and field results", *Journal of Electromagnetic Waves and Applications*, vol. 34, no. 14, pp. 1930-1954, 2020.

[24] A. E. -C. Tan, J. McCulloch, W. Rack, I. Platt and I. Woodhead, "Radar Measurements of Snow Depth Over Sea Ice on an Unmanned Aerial Vehicle," *IEEE Transactions on Geoscience and Remote Sensing*, vol. 59, no. 3, pp. 1868-1875, 2021.

[25] R. O. R. Jenssen, M. Eckerstorfer and S. Jacobsen, "Drone-Mounted Ultrawideband Radar for Retrieval of Snowpack Properties," *IEEE Transactions on Instrumentation and Measurement*, vol. 69, no. 1, pp. 221-230, 2020.

[26] R. O. R. Jenssen and S. K. Jacobsen, "Measurement of Snow Water Equivalent Using Drone-Mounted Ultra-Wide-Band Radar," *Remote Sensing*, vol. 13, no. 13, p. 2610, Jul. 2021.

[27] Kanagaratnam, P. (2002). "Airborne radar for high resolution mapping of internal layers in glacial ice to estimate accumulation rate" (Order No. 3069058). Available from ProQuest Dissertations & Theses Global. (305582805).

[28] B. Y. Mills, A. G. Little, K. V. Sheridan and O. B. Slee, "A High Resolution Radio Telescope for Use at 3.5 M," in Proceedings of the IRE, vol. 46, no. 1, pp. 67-84, Jan. 1958, doi: 10.1109/JRPROC.1958.286712.

[29] J. A. Nunn et al., "A Lightweight Planar Ultrawideband UHF Monopole Mills Cross Array for Ice Sounding," in IEEE Antennas and Wireless Propagation Letters, vol. 19, no. 7, pp. 1197-1200, July 2020, doi: 10.1109/LAWP.2020.2995079.

[30] C. Degel *et al.*, "3D sonar system based on mills cross antenna configuration," *2014 Oceans - St. John's*, 2014, pp. 1-6, doi: 10.1109/OCEANS.2014.7003133.

[31] Catalog of Window Taper Functions for Sidelobe Control, SANDIA REPORT SAND2017-4042

[32] Anatomy of a SAR impulse response, SANDIA REPORT SAND2017-5042

[33] Curt Peek, 'Estimation and compensation of frequency sweep nonlinearity in FMCW radar', Master's Thesis, University of Twente, https://purl.utwente.nl/essays/69455 (Accessed on:08/09/2022)

[34] Phase Noise Application Note - Vectron International https://www.vectron.com/products/literature_library/phase_noise.pdf (Accessed on:08/09/2022)

[35] F. Abushakra et al., "Ultra-Wideband Coplanar Vivaldi Antenna Array with Dielectric Patch Antenna for Grating Lobes Suppression," in *IEEE Access*, vol. 10, pp. 54410-54420, 2022, doi: 10.1109/ACCESS.2022.3175840.

[36] P. V. Brennan, Y. Huang, M. Ash and K. Chetty, "Determination of Sweep Linearity Requirements in FMCW Radar Systems Based on Simple Voltage-Controlled Oscillator Sources," in *IEEE Transactions on Aerospace and Electronic Systems*, vol. 47, no. 3, pp. 1594-1604, July 2011, doi: 10.1109/TAES.2011.5937252.

[37] R. O. R. Jenssen, M. Eckerstorfer and S. Jacobsen, "Drone-Mounted Ultrawideband Radar for Retrieval of Snowpack Properties," in *IEEE Transactions on Instrumentation and Measurement*, vol. 69, no. 1, pp. 221-230, Jan. 2020, doi: 10.1109/TIM.2019.2893043.

[38] M. Tiuri, A. Sihvola, E. Nyfors and M. Hallikaiken, "The complex dielectric constant of snow at microwave frequencies," in *IEEE Journal of Oceanic Engineering*, vol. 9, no. 5, pp. 377-382, December 1984, doi: 10.1109/JOE.1984.1145645.

[39] USDA Natural Resources Conservation Service National Water and Climate Center, Mesa Lakes (622) Colorado SNOTEL Site records (https://wcc.sc.egov.usda.gov/) (Accessed on:08/09/2022)

[40] A.K. Fung and H. Eom, Coherent Scattering of a Spherical Wave from an Irregular Surface, *IEEE Transactions on Antennas and Propagation*, VOL. AP-31, NO. *1,* JANUARY *1983*

[41] J. Li *et al.*, "Coherent and incoherent clutter reduction techniques to sound ice from high altitudes," *EUSAR 2012; 9th European Conference on Synthetic Aperture Radar*, 2012, pp. 243-246.

[42] U. Nielsen and J. Dall, "Direction-of-Arrival Estimation for Radar Ice Sounding Surface Clutter Suppression," in *IEEE Transactions on Geoscience and Remote Sensing*, vol. 53, no.

9, pp. 5170-5179, Sept. 2015, doi: 10.1109/TGRS.2015.2418221.

[43] J. Li *et al*., "High-Altitude Radar Measurements of Ice Thickness Over the Antarctic and Greenland Ice Sheets as a Part of Operation IceBridge," in *IEEE Transactions on Geoscience and Remote Sensing*, vol. 51, no. 2, pp. 742-754, Feb. 2013, doi: 10.1109/TGRS.2012.2203822.

Shriniwas Kolpuke received his B.E. degree in Electronics Engineering from Swami Ramanand Teerth Marathwada University Nanded, India, in 2011. He received his M.S. in VLSI and Embedded System Design from Jawaharlal Nehru Technological University Hyderabad, India, in 2013 and his M.S. in Aerospace Engineering from the University of Kansas, Lawrence, in 2017. He is now working towards his Ph.D. in Aerospace Engineering and Mechanics at the University of Alabama, Tuscaloosa. His research focuses on the design, development, and optimization of FMCW radars for snow and soil moisture measurements.

Christopher Simpson received his B.S. in Aeronautics and Astronautics Engineering from Purdue University in 2010. He received his M.S. in Aerospace Engineering and Mechanics in 2016 from The University of Alabama, where he is currently enrolled as a Ph.D. student in Aerospace Engineering and Mechanics. His research focuses on signal processing and the design and integration of remote sensing payloads on manned and unmanned aircraft.

Feras Abushakra received his B.Sc. degree in electrical engineering from the Jordan University of Science and Technology (JUST), Irbid, Jordan. He obtained his M.Sc. degree in wireless communication engineering from Al-Yarmouk University, Jordan, in 2017. He is currently working towards his Ph.D. degree in electrical and computer engineering at the University of Alabama (UA), Tuscaloosa. He is also a graduate research assistant at the Remote Sensing Center at UA. His research focus on UWB arrays, waveguides, and radar systems for earth remote sensing including soil moisture and snow depth measurements.

Abhishek K. Awasthi (S'11–M'19) completed his B. Tech. in Electronics and Communication Engineering from Ajay Kumar Garg Engineering College Ghaziabad (UPTU Lucknow), 2008. He earned his M. Tech. in Digital Communication from Ambedkar Institute of Technology Delhi (GGSIP University Delhi), 2011. He obtained his doctoral degree from the Department of Electrical Engineering (RF and Microwave) of the Indian Institute of Technology Kanpur in 2018. He worked as an Assistant Research Engineer at the Remote Sensing Center at the University of Alabama, Tuscaloosa. Currently he is working as Assistant Professor at Electrical Cluster at UPES Dehradun, India. His current research interests include phased antenna arrays and ultra-wideband radar systems.

Omid Reyhanigalangashi (S'19) received the B.Sc. degree in electrical engineering from Karaj Islamic Azad University, Alborz, Iran, in 2014, and the M.Sc. degree in electrical engineering from Qazvin Islamic Azad University, Qazvin, Iran, in 2017. From 2015 to 2019, he worked as a Project Engineer in FiberHome Telecommunication Technologies Co., Ltd., a globally renowned information and communication network product and solution provider. In August 2019, he joined the School of Electrical and Computer Engineering at the University of Alabama with a Research Assistantship (RA) to work toward a Ph.D. degree in electrical engineering. His research interests include field-programmable gate array (FPGA), digital signal processing (DSP), and embedded systems.

Jacob Pierce received the B.S. degree in aerospace engineering and mechanics from The University of Alabama in May of 2020 and the M.S. degree in aerospace engineering and mechanics from The University of Alabama in December of 2021. He served as a Graduate Research Assistant at The University of Alabama Remote Sensing Center from May 2020 to December 2021 and continues to work there as a Research Aide. His research interests include FMCW and pulsed radar technologies, signal processing, software development, estimation theory, and aircraft controls.

Tuan Luong received a B.S degree in Aerospace Engineering from the University of Alabama in 2021 and earned his M.Sc. degree in Aerospace Engineering at the University of Alabama in 022. He is currently pursuing a PhD degree in Aerospace Engineering. Since 2019, he has been an Undergraduate Research Assistant with the Remote Sensing Center, The University of Alabama. He also began working for the Laboratory for Autonomy, GNC, and Estimation Research in 2020.His research interests include control algorithm for unmanned systems, optimal state estimation and sensor fusion.

Jordan Larson is an Assistant Professor at the University of Alabama in the Department of Aerospace Engineering and Mechanics starting fall 2019 where he leads the Laboratory for Autonomy, GNC, and Estimation Research (LAGER) and serves as the sUAS team lead for the Remote Sensing Center (RSC) at the University of Alabama.

Dr. Larson received his Ph.D. from the Department of Aerospace Engineering and Mechanics at the University of Minnesota-Twin Cities. His research interests include autonomy, GNC, Unmanned Aircraft Systems (UAS), multi-agent systems, multi-target tracking, multi-sensor data fusion, and information risk analysis.

Drew Taylor received the B.S. and M.S. degrees in electrical engineering from the University of Alabama, Tuscaloosa, AL, USA, in 2008 and 2011, respectively, and the Ph.D. degree in electrical and computer engineering from Mississippi State University, Mississippi State, MS, USA, in 2018. He is currently an Assistant Professor of electrical and computer engineering with the Remote Sensing Center, University of Alabama, Tuscaloosa, AL, USA. His research interests include embedded systems, radar signal processing and remote sensing of the earth.

David Braaten received the B.S. degree in meteorology from the State University of New York, Oswego, NY, USA, in 1977, the M.S. degree in meteorology from San Jose State University, San Jose, CA, USA, in 1981, and the Ph.D. in atmospheric science from the University of California, Davis, CA, USA, in 1988.,He is currently a Professor with the Department of Geography and Atmospheric Science, University of Kansas (KU), Lawrence, KS, USA, where he has been teaching atmospheric science since 1989. He is associated with the Center for Remote Sensing of Ice Sheets, KU, with an interest in snow accumulation processes and ice sheet mass balance.

S. Prasad Gogineni (M'84–SM'92–F'99) is a Cudworth Professor of Engineering at the University of Alabama and the Director of the Remote Sensing Center. He was the founding Director of the NSF Science and Technology Center for Remote Sensing of Ice Sheets (CReSIS) at the University of Kansas from 2005 to 2016. Dr. Gogineni is an IEEE Fellow and served as Manager of NASA's polar program from 1997–1999. He received the Louise Byrd Graduate Educator Award at the University of Kansas and was a Fulbright Senior Scholar at the University of Tasmania in 2002. He has been involved with radar sounding and imaging of ice sheets for approximately 35 years and contributed to the first successful demonstration of SAR imaging of an ice bed through ice more than 3 km thick. He is also led the development of ultra-wideband radars for measuring the thickness of snow over sea ice and the mapping of internal layers in polar firm and ice.